Factors Affecting the Predictability of Hurricane Humberto (2007)

JASON A. SIPPEL

NASA Goddard Space Flight Center, Greenbelt, Maryland

FUQING ZHANG

Department of Meteorology, The Pennsylvania State University, University Park, Pennsylvania

(Manuscript received 7 April 2009, in final form 19 January 2010)

ABSTRACT

This study uses ensemble Kalman filter analyses and short-range ensemble forecasts to study factors affecting the predictability of Hurricane Humberto, which made landfall along the Texas coast in 2007. Humberto is known for both its rapid intensification and extreme forecast uncertainty, which makes it an ideal case in which to examine the origins of tropical cyclone strength forecast error. Statistical correlation is used to determine why some ensemble members strengthen the incipient low into a hurricane and others do not. During the analysis period, it is found that variations in midlevel moisture, low-level convective instability, and strength of a front to the north of the cyclone likely lead to differences in net precipitation, which ultimately leads to storm strength spread. Stronger storms are favored when the atmosphere is more moist and unstable and when the front is weaker, possibly because some storms in the ensemble begin entraining cooler and drier postfrontal air during this period. Later during the free forecast, variable entrainment of postfrontal air becomes a leading cause of strength spread. Surface moisture differences are the primary contributor to intensity forecast differences, and convective instability differences play a secondary role. Eventually mature tropical cyclone dynamics and differences in landfall time result in very rapid growth of ensemble spread. These results are very similar to a previous study that investigated a 2004 Gulf of Mexico low with a different model and analysis technique, which gives confidence that they are relevant to tropical cyclone formation and intensification in general. Finally, the rapid increase in forecast uncertainty despite relatively modest differences in initial conditions highlights the need for ensembles and advanced data assimilation techniques.

1. Introduction

Understanding the source of uncertainty in tropical cyclone intensity forecasts continues to be a significant concern, especially given their recent lack of improvement (e.g., Franklin 2005; Elsberry et al. 2007). Predictions of tropical cyclone formation, rapid intensification, and decay remain particularly problematic (Houze et al. 2007), yet our knowledge on how error grows in such forecasts remains very limited (Van Sang et al. 2008). A better understanding of this problem can potentially lead to improved forecasts and is the motivation of the current study.

One storm that strongly highlights current problems forecasting genesis and intensity change is Hurricane Humberto, which rapidly formed off the upper Texas coast on the morning of 12 September 2007 (Fig. 1). The system was operationally declared a tropical depression at 1500 UTC, although the best-track postevent analysis issued by the National Hurricane Center (NHC) estimates that the depression had formed by 0900 UTC and that the system was a 17.5 m s^{-1} tropical storm by 1200 UTC. By the time of its landfall east of High Island, Texas, at 0700 UTC 13 September, the storm had strengthened to a 40 m s^{-1}, Category 1 hurricane. Thus, the cyclone intensified by approximately 22.5 m s^{-1} in the 19 h before its landfall, which makes it the most rapidly intensifying, near-landfall storm in U.S. records.

Humberto's development and evolution posed serious operational forecast challenges since all operational models failed to capture the storm's rapid genesis and intensification. For example, Zhang et al. (2009) demonstrated the severity of the failure of multiple real-time forecasts by the operational Global Forecast System (GFS) running at the National Centers for Environmental Prediction (NCEP). They also showed that the

Corresponding author address: Dr. Jason A. Sippel, NASA GSFC, Code 613.1, Greenbelt, MD 2077.
E-mail: jason.sippel@nasa.gov

DOI: 10.1175/2010JAS3172.1

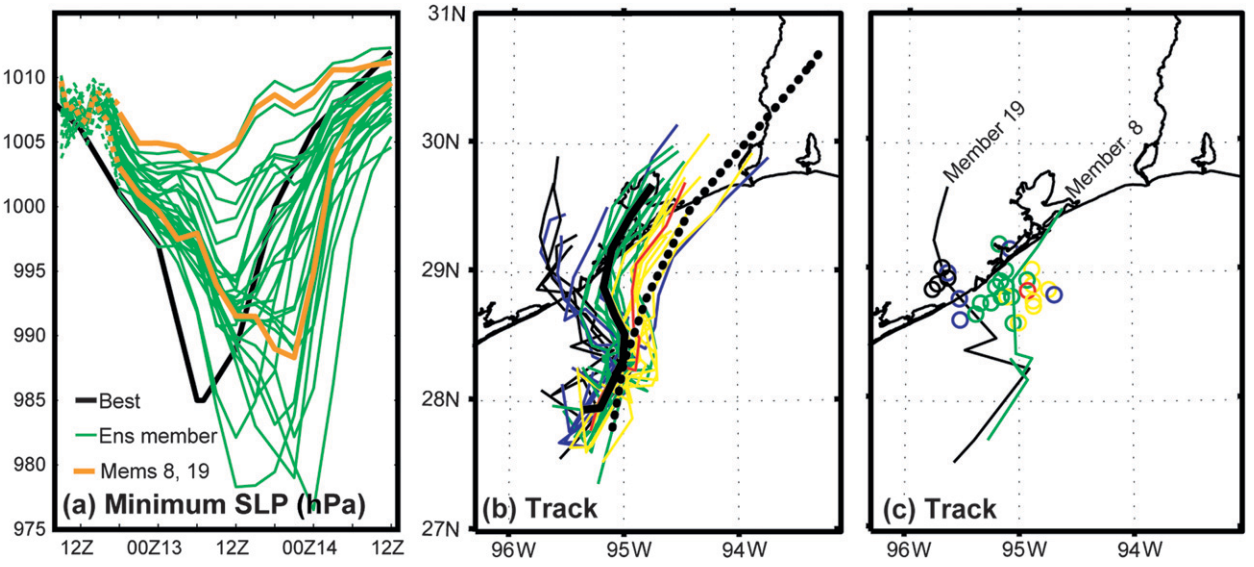

FIG. 1. The observed and ensemble forecast (a) intensity and (b),(c) track of Hurricane Humberto. In (a) the best-track postanalysis intensity estimate (black) is compared with time evolution of SLP from individual members of the EnKF analysis (green dashed) and subsequent ensemble forecast (green solid). In addition, members 8 and 19 are highlighted in orange. In (b), tracks of all ensemble members (thin black or colored lines), the ensemble mean position (thick black solid line), and the best-track postanalysis (thick black dotted line) are plotted every 3 h from 1200 UTC 12 Sep to 1500 UTC 13 Sep. In (c) the tracks of members 8 and 19 are shown with the 0600 UTC 13 Sep forecast position of all members (circles). Color represents maximum intensity of the cyclone for the given member (black: <25 m s^{-1}, blue: <30 m s^{-1}, green: <35 m s^{-1}, yellow: <40 m s^{-1}, and red: >40 m s^{-1}). Before 1800 UTC 12 Sep, position is calculated from the EnKF analysis, and thereafter it is calculated from the ensemble forecast.

Weather Research and Forecasting (WRF) model failed in postevent, 4.5-km, cloud-resolving simulations that were initialized with GFS analyses. Furthermore, the failure of operational models to capture the rapid intensification of Humberto led to large operational intensity forecast errors. Although tropical weather outlooks issued by the NHC mentioned the preceding disturbance for several days prior to Humberto's genesis, none mentioned the possibility that depression formation was imminent. Ultimately, the average 12-h intensity forecast error was 300% of long-term average intensity error with the same lead time.

To better understand how such error arises in tropical cyclone intensity forecasts, Sippel and Zhang (2008, hereafter SZ08) and Zhang and Sippel (2009, hereafter ZS09) used mesoscale ensembles and sensitivity experiments to investigate intensity forecast uncertainty in a nondeveloping Gulf of Mexico low. SZ08 found that variations in convective available potential energy (CAPE) and moisture through a deep layer were two factors that strongly influenced the genesis forecast. Ensemble members with higher initial values of these two variables had heavier subsequent precipitation, which caused their cyclones to strengthen more quickly. The resulting intensity differences between cyclones in different ensemble members increased owing to differences in oceanic heat fluxes and the extent to which mature tropical cyclone dynamics were reached (e.g., Emanuel 1986; Rotunno and Emanuel 1987). Meanwhile, ZS09 investigated the same low and found that differences in initial conditions much smaller than current observation and analysis error can cause very large differences in convection and ultimately determine whether or not a tropical cyclone forms. The strong sensitivity of precipitation (and thus cyclone strength) to small changes in initial conditions observed in SZ08 and ZS09 is consistent with previous findings regarding the negative influence of moist convection on atmospheric predictability (Islam et al. 1993; Olson et al. 1995; Zhang et al. 2002, 2003, 2006, 2007; Zhang 2005; Bei and Zhang 2007).

The result in SZ08 and ZS09 that CAPE contributed to cyclogenesis warrants further study. Generally speaking, convective instability is not believed to contribute to tropical cyclone genesis and intensification, especially compared to midlevel moisture, shear, sea surface temperature, and preexisting vorticity (E. Zipser 2009, personal communication). The recent study of Nolan et al. (2007) concurred with that sentiment, finding that there is no relationship between CAPE and the rate of cyclogenesis in an otherwise favorable environment. In addition, some studies (e.g., Kerns and Zipser 2009) have elected not to use a convective instability parameter to statistically discriminate developing from nondeveloping tropical disturbances. This practice is based partly on the

observational finding that the areal extent of precipitation is a better predictor of future tropical cyclone strength than the intensity of convection (Cecil and Zipser 1999). However, the modeling study of Montgomery et al. (2006) hypothesized that CAPE plays a role in the intensification of vortical hot towers (VHTs), which are known to help build the tropical cyclone vortex (Hendricks et al. 2004). Also, in 2003 a crude representation of atmospheric stability was added to the operational Statistical Hurricane Intensity Prediction System (SHIPS), which makes statistical–dynamical predictions of hurricane intensity (DeMaria et al. 2005). Thus, some clarification is needed to elucidate the extent to which convective instability hastens tropical cyclone formation.

This study, which is intended as a follow-up to test the results of SZ08 and ZS09, will investigate a few of the factors that led to the extreme forecast errors associated with Hurricane Humberto. In particular, we examine the control ensemble Kalman filter (EnKF) analyses of Weather Surveillance Radar-1988 Doppler (WSR-88D) observations from Zhang et al. (2009) in addition to a WRF ensemble forecast initialized from an EnKF analysis and briefly described in their section 3.4. Further information on data and methodology is given in section 2, and an overview of the genesis environment is presented in section 3. Section 4 examines the ensemble performance and predictability of the event, while section 5 examines factors that affected Humberto's predictability. A summary and discussion are presented in section 6.

2. Data and methodology

This investigation employs methodology originally developed in Zhang (2005) and Hawblitzel et al. (2007) and refined in SZ08 by investigating forecast sensitivity using an ensemble forecast. A similar method has also been used by Hakim and Torn (2008) to study the dynamics of midlatitude cyclones and by Torn (2010) to study an African easterly wave.

a. Forecast model and data assimilation methods

The control EnKF-WRF analyses and an ensemble forecast from Zhang et al. (2009) are used here, and a brief synopsis of the setup follows [see Zhang et al. (2009) for full details of the EnKF-WRF setup and performance]. The outer, 40.5-km WRF domain covers the contiguous United States with 160 × 121 grid points, and two nested domains cover the south-central United States and northern Gulf of Mexico with 160 × 121 (253 × 253) grid points and a grid spacing of 13.5 (4.5) km (see Fig. 2 of Zhang et al. 2009). All model domains have 35 vertical layers, and the model top is set at 10 hPa. Random, balanced, large-scale perturbations are added to NCEP GFS analyses at 0000 UTC 12 September to create initial conditions for a 30-member ensemble forecast that is integrated forward until 0900 UTC. Data assimilation of thinned and quality-controlled radial velocity observations from the Corpus Christi (KCRP) and Houston–Galveston (KHGX) radars begins at 0900 UTC. Assimilation proceeds in hourly cycles until 1800 UTC 12 September, at which point an EnKF-initialized ensemble forecast is integrated forward.

Sea surface temperatures are prescribed according to the skin temperature of the GFS analysis at 0000 UTC 12 September, which might affect results. Fixed skin temperatures can overestimate the effective mean temperature of the ocean mixed layer, which could artificially increase cyclone strength. Also, tropical cyclones have been observed to decrease sea surface temperatures from 1° to ~6°C (Black 1983; Bender et al. 1993) in their wakes. However, in the case of Humberto, the small size of the storm and short amount of time that higher winds were actually over the ocean surface likely minimized the immediate impact to storm intensity. Indeed, similar development of Humberto was achieved in another EnKF analysis and forecast experiment (not shown) in which sea surface temperatures were updated hourly with U. S. Navy mesoscale analyses.

The use of an EnKF for the analyses here is a major difference from the methodology of SZ08. In the analysis of SZ08, a cold-start technique was used, which possibly resulted in some artificial overreaction of initial convection to ambient convective instability during the model spinup period. For example, precipitation totals in SZ08 were generally considerably higher during the first 12 h than at later times, especially for those members with higher CAPE and/or midlevel moisture (e.g., their Fig. 12). This same trend was noted in the sensitivity study of ZS09 (e.g., their Fig. 7). The possibility that model spinup affected the results in SZ08 and ZS09 is further motivation for the current work in which the so-called ''hot-start'' EnKF analyses contains active moist convection.

b. Correlation analysis

As in SZ08, linear correlation is used here with correlation thresholds of 0.3, 0.5, and 0.7 and verbal descriptions of ''weak,'' ''moderate,'' and ''strong.'' Since the size of the ensemble used here is larger (i.e., 30 versus 20 members), confidence that a particular level of correlation is statistically different from 0 is higher (the three thresholds are significant with roughly 90%, 99.5%, and 99.99% confidence, respectively). Although it is well understood that correlation does not imply causality, it can be used to demonstrate that ensemble behavior is consistent with physical reasoning developed in other studies.

This study makes frequent use of part (also known as semipartial) correlation to elucidate relationships when multiple variables are correlated to one another. In SZ08 this method was alternatively referred to as statistical control and to first order it correlates two variables while effectively holding a third variable constant. For example, if variables x, y, and z are all correlated, then $(x{:}y)$ is the correlation between x and y, and $(x{:}y|z)$ is the first-order part correlation between x and y with z held constant. To calculate this in SZ08, linear regression between y and z was first used to predict values of y given z, and x was then correlated to the residuals between the actual and predicted values of y. Here, more general iterative equations (equivalent to the above for the first order) are used for first- and second-order part correlation, respectively:

$$(x{:}y|z_1) = \frac{(x{:}y) - (x{:}z_1)(y{:}z_1)}{\sqrt{1 - (y{:}z_1)^2}} \quad (1)$$

and

$$(x{:}y|z_1, z_2) = \frac{(x{:}y|z_1) - (x{:}z_2|z_1)(y{:}z_2|z_1)}{\sqrt{(1 - (y{:}z_2|z_1)^2}}. \quad (2)$$

If needed, even higher order part correlation can be calculated from the iterative procedure used to calculate (2) from (1). In a simple example, we use the first-order part correlation to test the sensitivity of storm intensity (y) at a later time to a particular field (x) given storm intensity (z) at the time of x.

Investigating which variables early in the genesis phase are well correlated with the intensity of the mature cyclone is useful because it reveals the factors that favor intensification and increase ensemble spread. Abiding by the SZ08 convention, here we define the intensity metric SLP_f (to avoid repetitions of long strings of similar words, this study makes use of many acronyms, a list of which along with their meanings can be found in Table 1), which is area-average sea level pressure (SLP) within 20 km of the cyclone center at 0600 UTC 13 September. This time is useful because it is before most ensemble members make landfall, and the intention is for landfall to not impact the observed correlation structure. However, the results are very similar with a slightly later time when the mean strength is higher but more ensemble members have storms that have made landfall. Finally, as in SZ08 the negative of SLP_f will be used in correlation computations so that positive correlation with SLP_f implies that a factor favors intensification.

The metric that we use for intensity at times before 0600 UTC 13 September is 1-km potential vorticity (PV) within 50 km of the center (hereafter PV_1). This is especially important for analysis during the data assimilation period, when the time-lag SLP correlation is not particularly consistent from one time to the next. For the free forecast period after 1800 UTC 12 September, PV and SLP are generally well enough correlated that they can be used interchangeably to achieve similar results.

TABLE 1. Acronyms and their meanings.

SLP_f	Average SLP within 20 km of cyclone center at 0600 UTC 13 Sep
PV_1	Average 1-km PV within 50 km of cyclone center
PRCP3h	Average 3-h precipitation within specified isopleths and 200 km of cyclone center
$q_{v\mathrm{sfc}}$	Surface water vapor mixing ratio
$q_{v3\mathrm{km}}$	3-km water vapor mixing ratio
T_{diff}	Difference between 2-km temperature and surface temperature
T_{sfc}	Surface temperature

3. Synoptic overview and genesis environment

The environment immediately surrounding Hurricane Humberto was relatively favorable for genesis. The focus for convection prior to cyclone formation was an inverted trough at low to mid levels that manifested itself at the surface as a weak low (Fig. 2). This system had moved westward across the Gulf of Mexico during the preceding week, and the NHC recognized it as a potential trigger for cyclogenesis as early as the afternoon of 10 September. Convection associated with the disturbance had access to modest convective instability (Fig. 2c), and it gradually became more widespread and organized preceding Humberto's genesis (Fig. 3). In addition, by 0900 UTC 12 September the local genesis environment had a deep layer of moist air (Figs. 2a,b,e) with relative humidity exceeding 85% through 5 km (not shown), which is a necessary genesis ingredient according to Rotunno and Emanuel (1987) and Emanuel (1989). Finally, the ample convection in the genesis region likely helped reduce upper-level PV and build an upper-level ridge above the circulation center (Fig. 2d). Associated with the ridge was a minimum in 200–850-hPa vertical wind shear, and mean shear near the circulation center on 12 September was well below 12.5 m s^{-1}, which is favorable for intensification according to DeMaria et al. (2001).

Nevertheless, potentially unfavorable factors lingered on a larger scale. For example, cooler and drier continental air was not far north of the developing cyclone and it could certainly inhibit genesis if it entrained into the circulation. A synoptic front had entered the region during the previous days and helped to somewhat modify the inland air mass prior to Humberto's genesis. At 0600 UTC 11 September the front was accompanied by a line of convection and cold cloud tops over northern

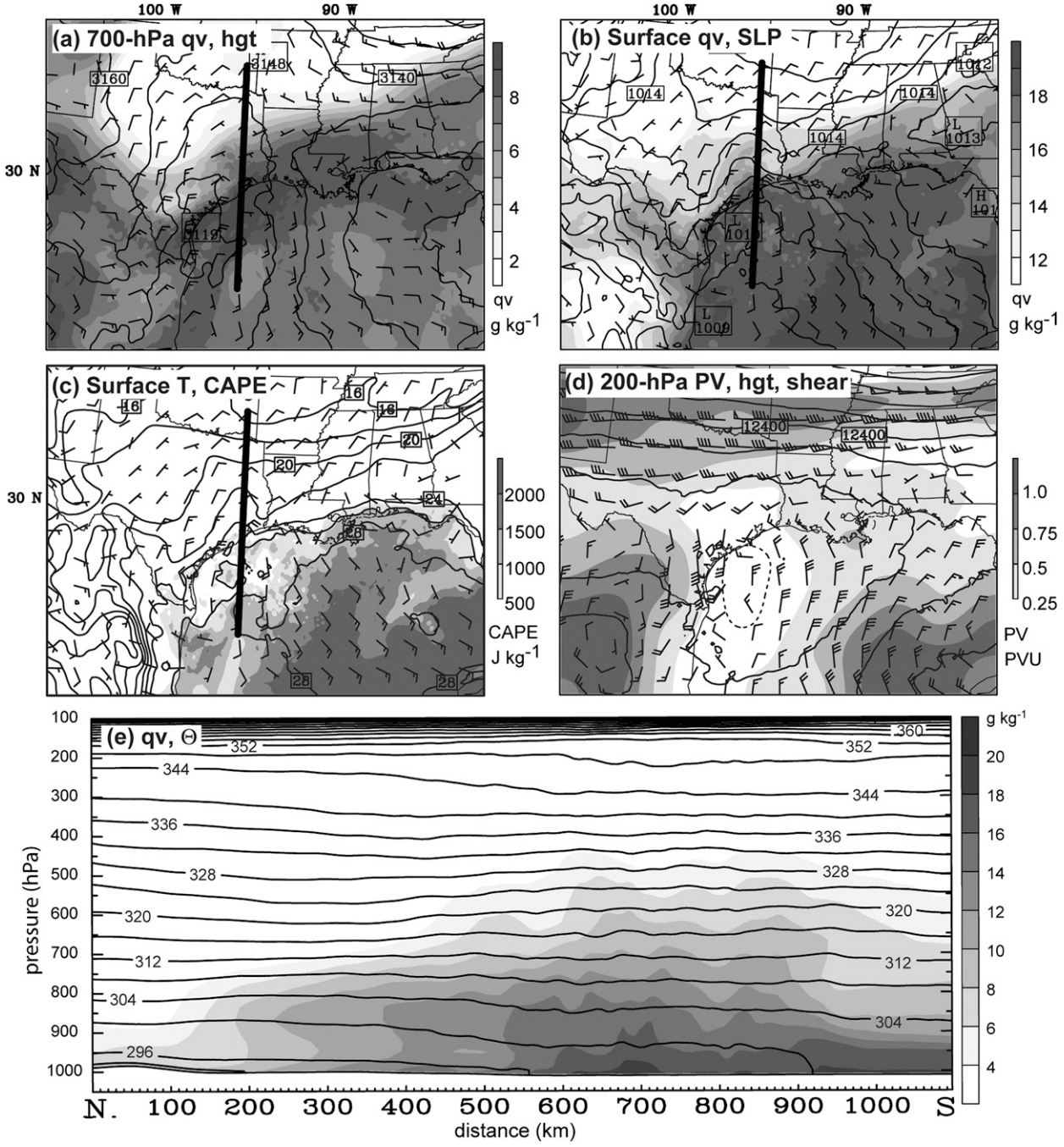

FIG. 2. The 0900 UTC 12 Sep EnKF analysis of thermodynamic, height, PV, wind, and shear fields: (a) 700-hPa mixing ratio (filled every 1 g kg^{-1}), height (contoured every 10 m), and wind (full barb represents 5 m s^{-1}), (b) surface mixing ratio, wind, and SLP (contoured every 1 hPa), (c) surface temperature (contoured every 2°C), wind, and MUCAPE (filled every 500 J kg^{-1}), and (d) 200-hPa height (contoured every 20 m), PV (smoothed, filled every 0.25 potential vorticity units for positive values and dash-contoured every 0.25 potential vorticity units for negative values), and 200–850-hPa shear (full barb represents 5 m s^{-1}), and (e) a cross section along the line in (a)–(c) of potential temperature (contoured every 4 K) and mixing ratio (filled every g kg^{-1}).

Texas (Figs. 3a and 4a), and the air mass over central and southern Texas was warm and humid. The temperature gradient along the coast, likely the result of stronger nocturnal cooling over land than over the Gulf of Mexico, was not associated with the front. The frontal boundary moved south throughout the day of 11 September (Fig. 3b), and by 0600 UTC 12 September the leading edge of cooler, drier air was draped across the Texas coastal plain

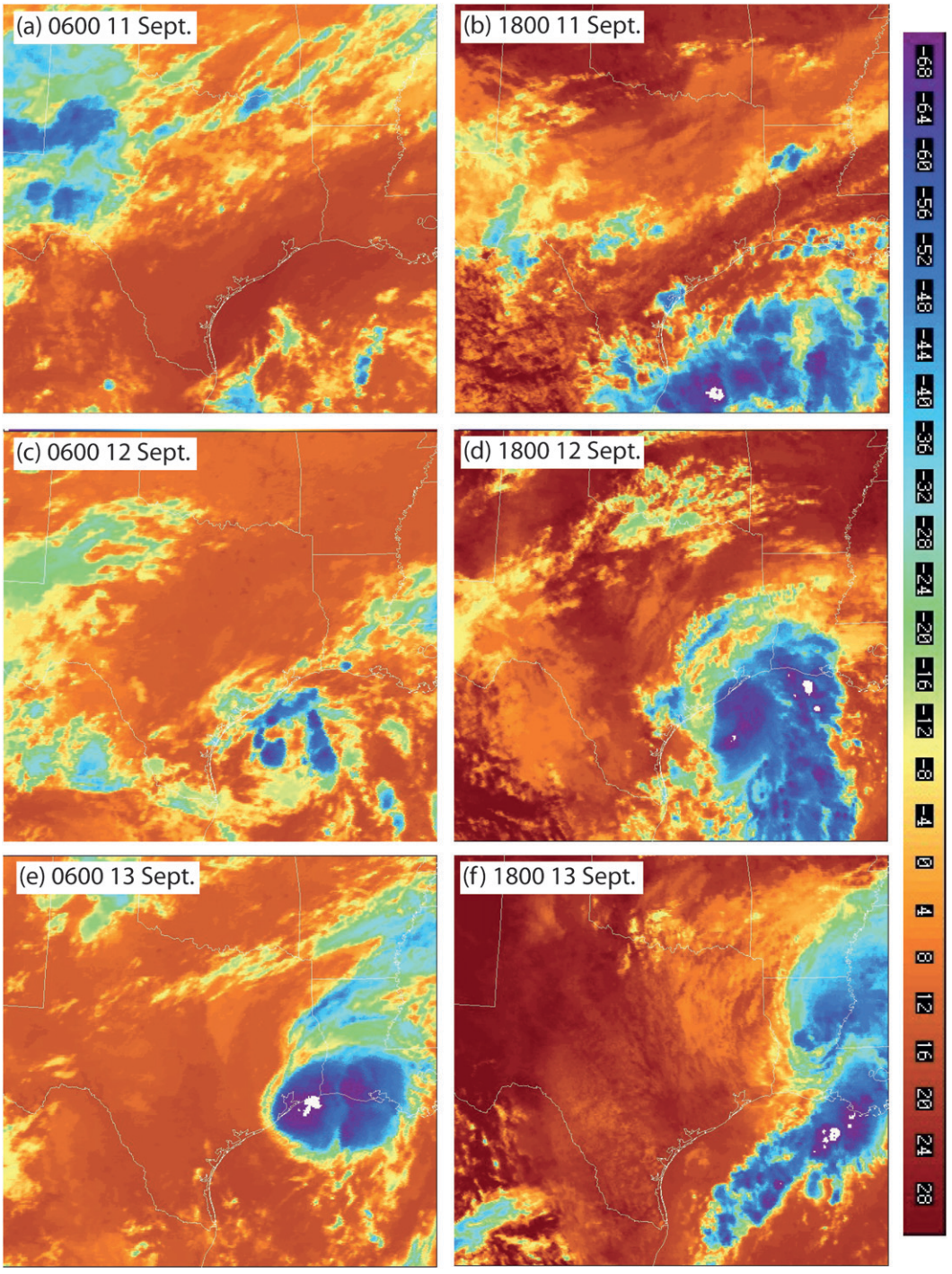

FIG. 3. Enhanced infrared imagery every 12 h from (a) 0600 UTC 11 Sep to (f) 1800 UTC 13 Sep. Images courtesy of www.rap.ucar.edu/weather/satellite.

(Fig. 4b). Although the air mass behind the front was clearly modified from 11 to 12 September, the region from central Texas to near the coast was slightly cooler and drier by 12 September than it had previously been (cf. Figs. 4a,b). The 0900 UTC EnKF analysis in Fig. 2 captures the distinct moisture and instability gradient along the Texas coast, but it also demonstrates the weakened state of the front. For example, potential temperature differences across the boundary were fairly small and generally confined to below 850 hPa (Fig. 2e). Nevertheless,

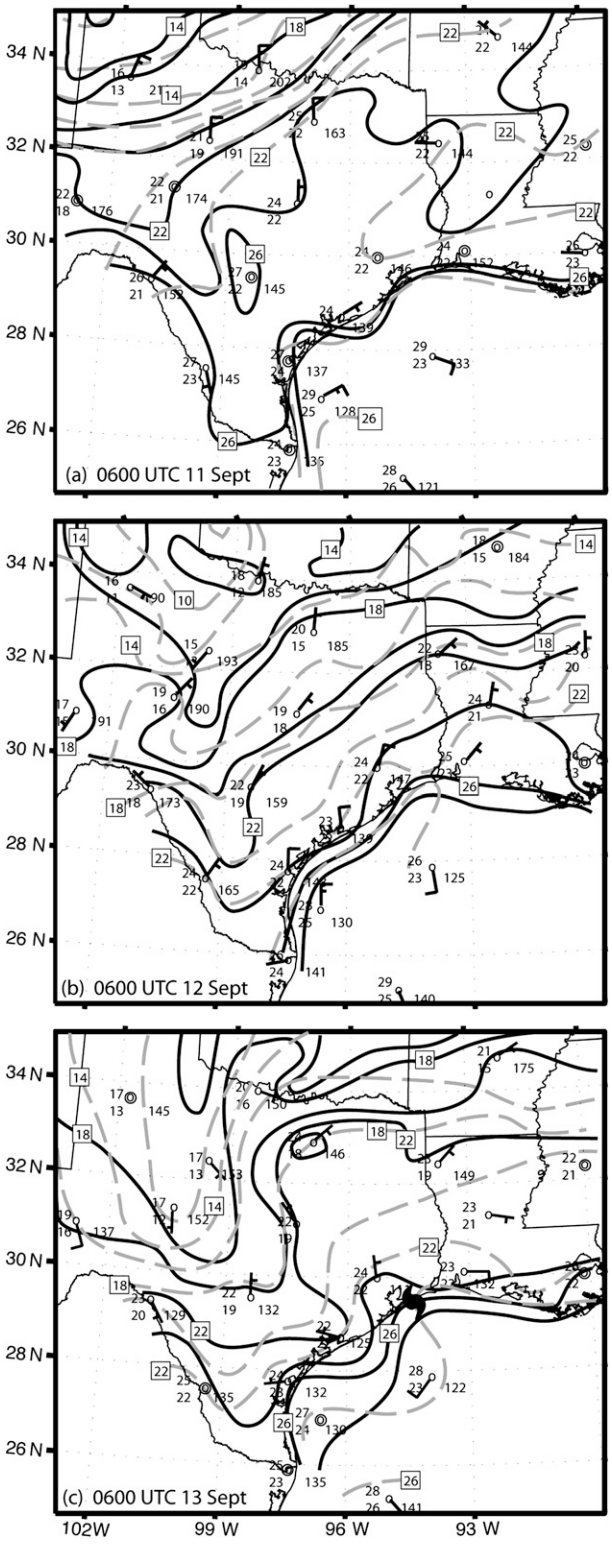

FIG. 4. Surface analyses of temperature (solid, every 2°C) and dewpoint (dashed, every 2°C) at (a) 0600 11 Sep, (b) 0600 12 Sep, and (c) 0600 13 Sep. Select observations are shown, but many more were used in the analysis. The black hurricane symbol in (c) represents the position of Humberto.

the leading edge of the modified surface air apparently encroached into the western part of Humberto's circulation as the storm made landfall (Figs. 4c and 5a), which might explain the lack of convection on the southwest side of the storm in both satellite (Figs. 3d–f) and radar (Fig. 6a) imagery. Finally, the 0900 UTC 12 September EnKF analysis shows that additional drier pockets at 700 hPa were also farther south over the Gulf of Mexico (Figs. 2a,e), and they too could potentially hinder genesis.

4. Ensemble performance and predictability

Zhang et al. (2009) found that use of an EnKF could considerably benefit the prediction of Humberto. In particular, assimilation of radial velocity observations from three WSR-88D radars along the Gulf coast resulted in analyses that accurately depicted the storm's best-track position and intensity. In addition, EnKF-initialized deterministic (not shown) and ensemble (Fig. 1) forecasts outperformed operational forecasts by predicting the rapid formation and intensification of the hurricane.

Not only does this Zhang et al. (2009) ensemble capture the genesis and rapid intensification of Humberto, but forecasts from some individual members also reasonably depict Humberto's structure. To further demonstrate this, Figs. 6a,b compare observed reflectivity from the time around Humberto's landfall with derived 2-km reflectivity[1] from member 8, which has a relatively strong storm for the period of interest in this study. The simulated reflectivity in member 8 generally represents the central structure of Humberto with a well-organized central core and a 50% closed eyewall. In terms of minimum SLP, it is somewhat weaker than Humberto at its landfall, but other storms in the ensemble do obtain lower central pressure (see Fig. 1a).

In addition, certain members also accurately demonstrate the storm's interaction with the continental air. For instance, Fig. 5a shows a mesoscale surface analysis zoomed in on Humberto's landfall, and Fig. 5b shows the corresponding member-8 forecast. The forecast temperature field in Fig. 5b exhibits a very similar wavelike pattern to that observed in Fig. 5a, and the temperature difference from the tropical to the continental air is about the same in both panels. Finally, a wavelike field in simulated surface moisture (not shown) is also similar to that seen in the surface observations.

One noticeable problem with all members in Fig. 1 is that they strengthen the storm too slowly. This is especially true for members like 19 (Fig. 6c), which does a mediocre job at representing Humberto's intensity and

[1] Reflectivity is calculated with Read-Interpolate-Plot, version 4 (RIP4), based on the mixing ratios of rain, snow, and graupel.

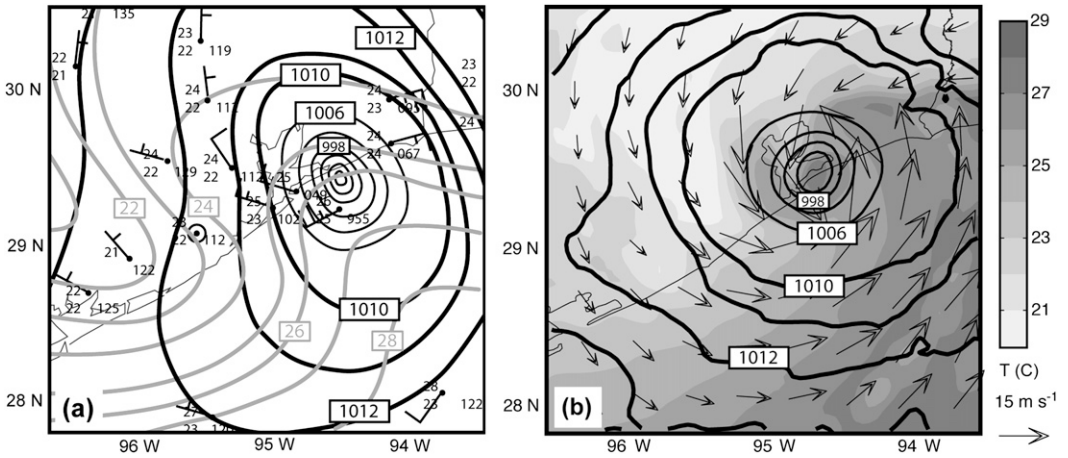

FIG. 5. A mesoscale view of Humberto's landfall from both the (a) observed and (b) modeling perspectives. The analysis in (a) is at 0600 UTC 13 Sep and utilizes data from outside the displayed domain and at both earlier and later times for consistency. The central position and minimum pressure of the cyclone are determined from the NHC post-analysis valid at the same time. Full wind barbs represent 5 m s^{-1} and analyzed fields are as follows: pressure is contoured every 4 hPa from 986 to 1006 hPa (thin black lines) and every 1 hPa at and above 1010 hPa (thick black lines), and temperature is contoured every 1°C. The forecast in (b) is taken from member 8 of the ensemble at 1500 UTC 13 Sep. Surface temperature is shaded every 1°C, pressure is contoured as in (a), and surface wind vectors are shown.

structure. While Humberto's actual central pressure falls below the lower limit of the ensemble envelope until its landfall, many ensemble members obtain a central pressure similar to the lowest observed with the storm because their simulated storms make landfall later. Yet, despite this error, all members perform better than did the operational models.

The ensemble captures Humberto's general track, but it moves the storm northeastward too slowly. For example, in Figs. 1b,c the actual position of the cyclone at 1500 UTC 13 September is well northeast of all the ensemble members. This error is partly a result of a slow left-of-track deviation that takes place after 1800 UTC 12 September (i.e., after the final EnKF analysis) in many of the ensemble members. This deviation might be the result of error present in the mean advective wind field of the environment, which is only weakly constrained by the Doppler radar observations. Ensemble members with the most severe deviation have storms that make landfall too early and far south, and in members with lesser deviation, the landfall location forecast is more accurate but 6–12 h too late (Fig. 1).

Despite the benefits of data assimilation, the very large ensemble intensity spread in Fig. 1a exemplifies the large

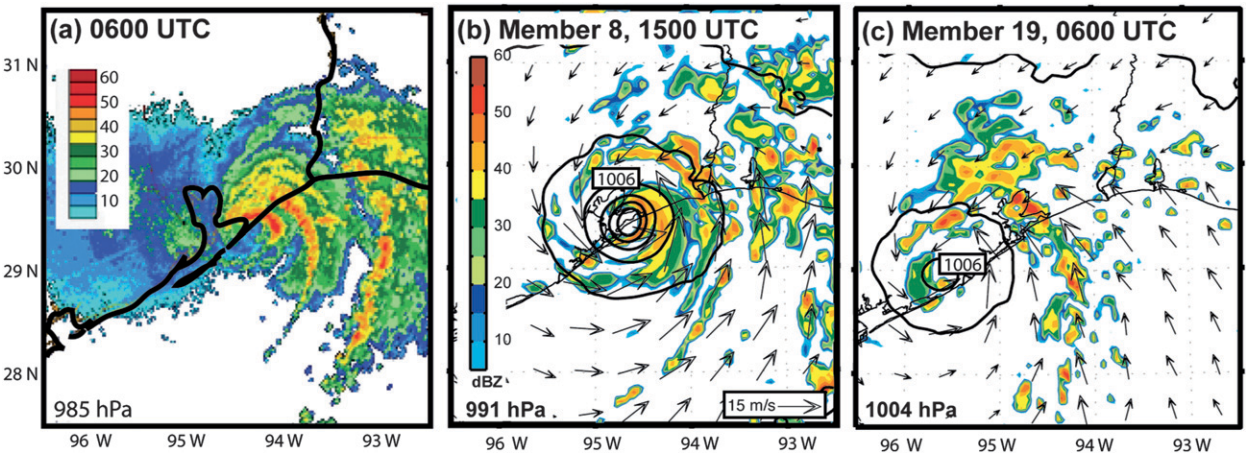

FIG. 6. Radar reflectivity from (a) the KHGX WSR-88D radar and (b),(c) the forecast around the time of Humberto's observed and simulated landfall on 13 Sep. Observed reflectivity in (a) is taken from the 0.5° elevation angle and derived reflectivity in (b) and (c) is taken from the 2-km level in ensemble members (b) 8 and (c) 19. All panels cover approximately the same domain, and surface wind vectors and SLP (contoured every 4 hPa) are also shown in (b) and (c) with the minimum central SLP in the bottom left corner.

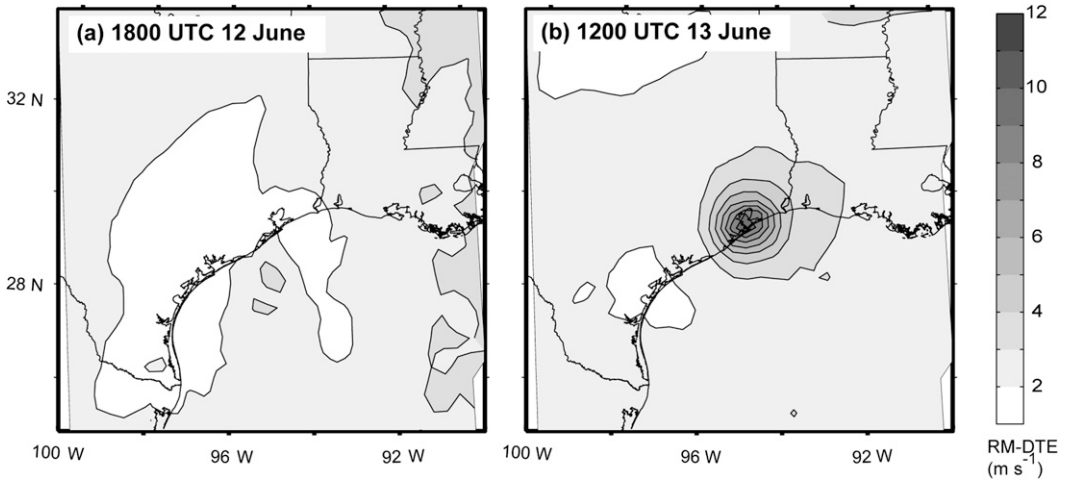

FIG. 7. RM-DTE (every 1 m s^{-1}) for the approximate area of domain 3 at (a) 1800 UTC 12 Sep and (b) 1200 UTC 13 Sep. Sampling is limited to every seven grid points (31.5 km) to facilitate comparison with Fig. 5 from SZ08, which shows RM-DTE sampled to a 30-km grid.

uncertainty associated with the intensity forecast of Hurricane Humberto. In fact, ensemble spread grows much more rapidly in the case of Humberto than in the 2004 Gulf low studied in SZ08 and ZS09. For instance, the minimum SLP envelope here spans nearly 30 hPa after 18 h of forecast time (i.e., by 1200 UTC 13 September in Fig. 1a), but the envelope in the gulf low was only 14 hPa after 36 h (when sampled on their 3.3-km grid, see Fig. 3 of ZS09). As a result of the larger intensity spread in the Humberto case, the root mean of difference total energy (RM-DTE)[2] error grows much faster. In Fig. 7, RM-DTE increases from about 3 m s^{-1} at 1800 UTC 12 September to over 10 m s^{-1} by 1200 UTC 13 September (to facilitate comparison to SZ08, RM-DTE in Fig. 7 has been sampled every seven grid points, or 31.5 km). This >300% RM-DTE increase occurs in only half the time of a similar percentage increase in SZ08 (see their Fig. 5). Thus, forecast uncertainty is considerably higher with Humberto than with the 2004 Gulf low. Ultimately, the presence of extreme spread with the relatively accurate ensemble-mean performance renders this an excellent case with which to test the results of SZ08.

5. Factors affecting predictability

This section divides the dynamical examination into two general time periods: one is from 0900 to 1800 UTC 12 September and the other is after 1800 UTC. The reason for doing this is that 1800 UTC marks the end of the data assimilation period and the beginning of the free ensemble forecast. Thus, the pre–1800 UTC period contains hourly adjustments associated with assimilation, whereas the forecast period is free of such adjustments. These adjustments can potentially affect the dynamic evolution in ways that might not be natural (e.g., through imbalance that initiates or strengthens convection, similar to the possible overreaction of precipitation to initial CAPE and moisture in SZ08), but they typically decrease in magnitude after multiple assimilation cycles (Snyder and Zhang 2003; Zhang et al. 2004). Therefore, statistically inferred dynamics are less likely to be artificially affected by the assimilation process nearer 1800 UTC. Furthermore, use of covariance relaxation means that an EnKF cycle only updates perturbations to the ensemble mean by 15%, keeping 85% of their previous value. Regardless, we only briefly examine ensemble evolution during the data assimilation period in light of the aforementioned caveat, and the main focus of this study is on the free ensemble forecast period.

It should be remembered that error in the ensemble-mean intensity and track might be associated with error in the statistically inferred dynamics as well. For instance, because the simulated intensification lags the observed intensification, it is likely that mature tropical cyclone dynamics commenced in nature sooner than they commence in the simulation. It is also possible that track error in most ensemble members results in different interaction between the cyclone and inland air than was actually observed. These errors are likely a result of error in the larger-scale analysis and in the forecast model, which is not examined here.

[2] Here difference total energy is defined as DTE = $0.5(u'u' + v'v' + kT'T')$ and $k = C_p/T_r$ (C_p = 1004.9 J kg^{-1} K^{-1} and T_r = 270 K). Primes denote differences between an ensemble member and the ensemble mean. See SZ08 for more details.

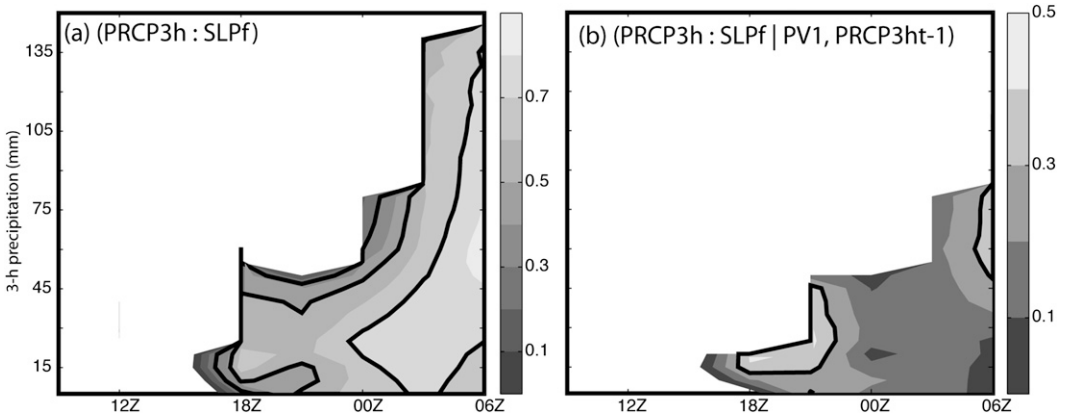

FIG. 8. Relationship between PRCP3h and SLP_f as a function of precipitation intensity and time between 0900 UTC 12 and 0600 UTC 13 Sep. (a) Correlation between PRCP3h and SLP_f and (b) part correlation controlling for antecedent PRCP3h and PV_1. Correlation greater than 0 is shaded; thresholds 0.3, 0.5, and 0.7 are outlined with a bold line. Differences in the shaded region between (a) and (b) are a result of the PRCP3h control in (b).

a. Data assimilation period: Vortex building and thermodynamics

To elucidate what builds the initial vortex and increases spread before 1800 UTC 12 September, we first examine the relationship between PV_1 (i.e., area-average 1-km PV), precipitation and SLP_f (i.e., area-average SLP just before landfall). The precipitation metric we use, which is average 3-h precipitation within certain ensemble-mean isopleths and 200 km of the center (hereafter PRCP3h), represents the net amount of latent heating for different precipitation intensities.[3] Figure 8a shows the direct correlation between PRCP3h and SLP_f, and to examine this relationship independent of previous precipitation and storm intensity, the second-order part correlation between SLP_f and PRCP3h (controlling for both antecedent PRCP3h and PV_1) is also shown in Fig. 8b. Thus, while Fig. 8a shows the relationship between precipitation and future intensity, Fig. 8b shows when precipitation is most likely to independently contribute to intensification. Furthermore, to better illustrate the spatial relationship between precipitation and PV during the vortex-building phase, Fig. 9 shows ensemble-mean 1-km PV and 3-h precipitation at 0900, 1200, 1500, and 1800 UTC 12 September.

Latent heating during the data assimilation period before 1800 UTC appears to increase low-level PV, and differences in latent heating affect the spread of both PV_1 and SLP_f. In Fig. 9, the PV anomaly present in the 0900 UTC analysis strengthens considerably amid the heavy precipitation [consistent with Haynes and McIntyre (1987)]. Most of the increase in PV occurs between 1500 and 1800 UTC when widespread heavy precipitation begins to fall and the ensemble-mean 1-km PV anomaly doubles in strength from 4 to 8 PVU (Figs. 9c,d). Concomitant with the increase in PV is weak part correlation between PRCP3h and SLP_f (Fig. 8b), which is independent of both prior precipitation and PV strength. Furthermore, when the precipitation metric is analyzed in hourly increments (not shown), weak to moderate part correlation between precipitation and SLP_f begins as early as 1100 UTC. Likewise, correlation between PV_1 and SLP_f increases steadily through the morning of 12 September (Fig. 9) and it becomes strong as precipitation grows heavier and the low-level PV anomaly dramatically intensifies.

Understanding that differences in net precipitation before 1800 UTC likely lead to variance in vortex strength, we now turn our attention to factors that might affect precipitation. Our focus will be on low to mid level thermodynamics, which SZ08 found to be the main factor that contributed to simulated cyclogenesis. Thus, Figs. 10a–d show ensemble-mean 3-km water vapor mixing ratio (hereafter $q_{v3\mathrm{km}}$), surface water vapor mixing ratio (hereafter $q_{v\mathrm{sfc}}$), most unstable CAPE (MUCAPE),[4] and the difference between surface and 2-km temperatures (a proxy for low-level convective instability, hereafter T_{diff}), and their respective second-order part correlation

[3] Generally similar results are obtained with slightly different metrics for both storm strength (i.e., PV) and precipitation, showing significant part correlation between SLP_f and precipitation between 1500 and 2100 UTC 12 September and again between 0300 and 0600 UTC 13 September.

[4] MUCAPE is computed as the CAPE for the parcel in each column with maximum equivalent potential temperature within the lowest 3000 m. Following the recommendation of Doswell and Rasmussen (1994), virtual potential temperature is used in this calculation.

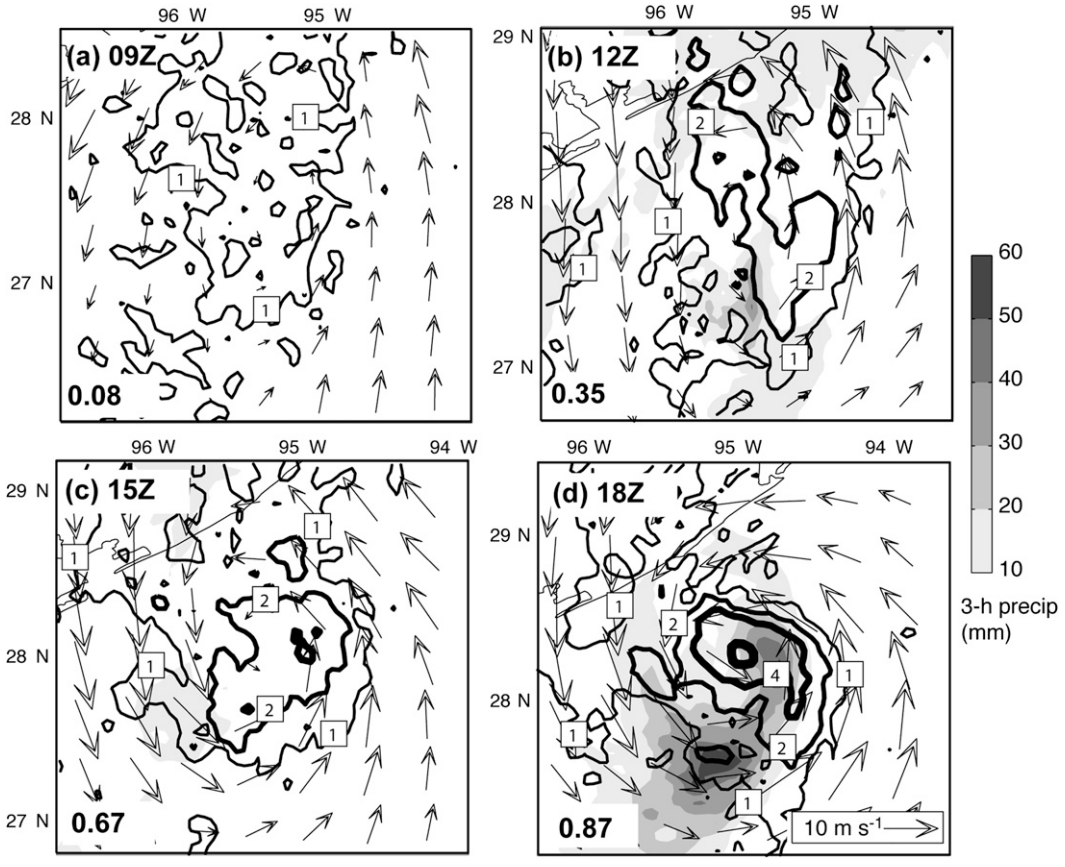

FIG. 9. Ensemble-mean 3-h precipitation (shaded every 10 mm), surface wind vectors, and 1-km PV (contoured at 1, 2, 4, and 8 PVU) valid at (a) 0900, (b) 1200, (c) 1500, and (d) 1800 UTC 12 Sep. Analysis is completed in a Lagrangian framework, and for spatial reference the map background is plotted so that the circulation center is located at the ensemble-mean position of the cyclone.

with SLP_f as a function of radius. Each variable is azimuthally averaged in a Lagrangian, storm-centered framework with 20-km annuli, and the correlation is computed after the average is taken. Furthermore, part correlation is calculated controlling for PV_1 and antecedent PRCP3h at the 5-mm threshold.

During the data assimilation period, the strongest predictors of future storm intensity in an area-average sense are low-level stability and 3-km moisture. From about 1200 to 1500 UTC average T_{diff} beyond 20 km from the center is weakly correlated with SLP_f (Fig. 10a), which suggests that more intense and widespread precipitation could be a result of higher near-surface instability. However, reservation must be used in interpreting this result early in the assimilation period because of the possible influence of EnKF adjustments. In addition to low-level instability, $q_{v3\text{km}}$ is weakly related to SLP_f in the 1500–1800 UTC time frame. The significant $q_{v3\text{km}}$ correlation in Fig. 10d moves radially inward with time, which suggests that SLP_f is sensitive to the moisture of midlevel air that is being drawn into the system as the vortex is built. This result is quite similar to that of SZ08, which showed initial midlevel moisture to be an important factor that influences genesis. Finally, a lack of concomitant positive part correlation between relative humidity and SLP_f (not shown) might suggest that the pathway from water vapor differences to strength variability herein goes directly through latent heating and is not related to the ability of high relative humidity to prevent cold downdrafts. This is also similar to the results of SZ08.

Expanding to a regional view, uncertainty in the strength of the front discussed in section 3 also appears to increase spread before 1800 UTC 12 September. To demonstrate this, Fig. 11 examines ensemble-mean $q_{v\text{sfc}}$ and surface temperature T_{sfc} and their respective part correlation with SLP_f at 1200 UTC 12 September (controlling for PV_1 and PRCP3h h within the ensemble-mean 5-mm isopleth). A feature common to these figure panels and intermittently present during the pre–1800 UTC period is weak to moderate correlation along and north of the

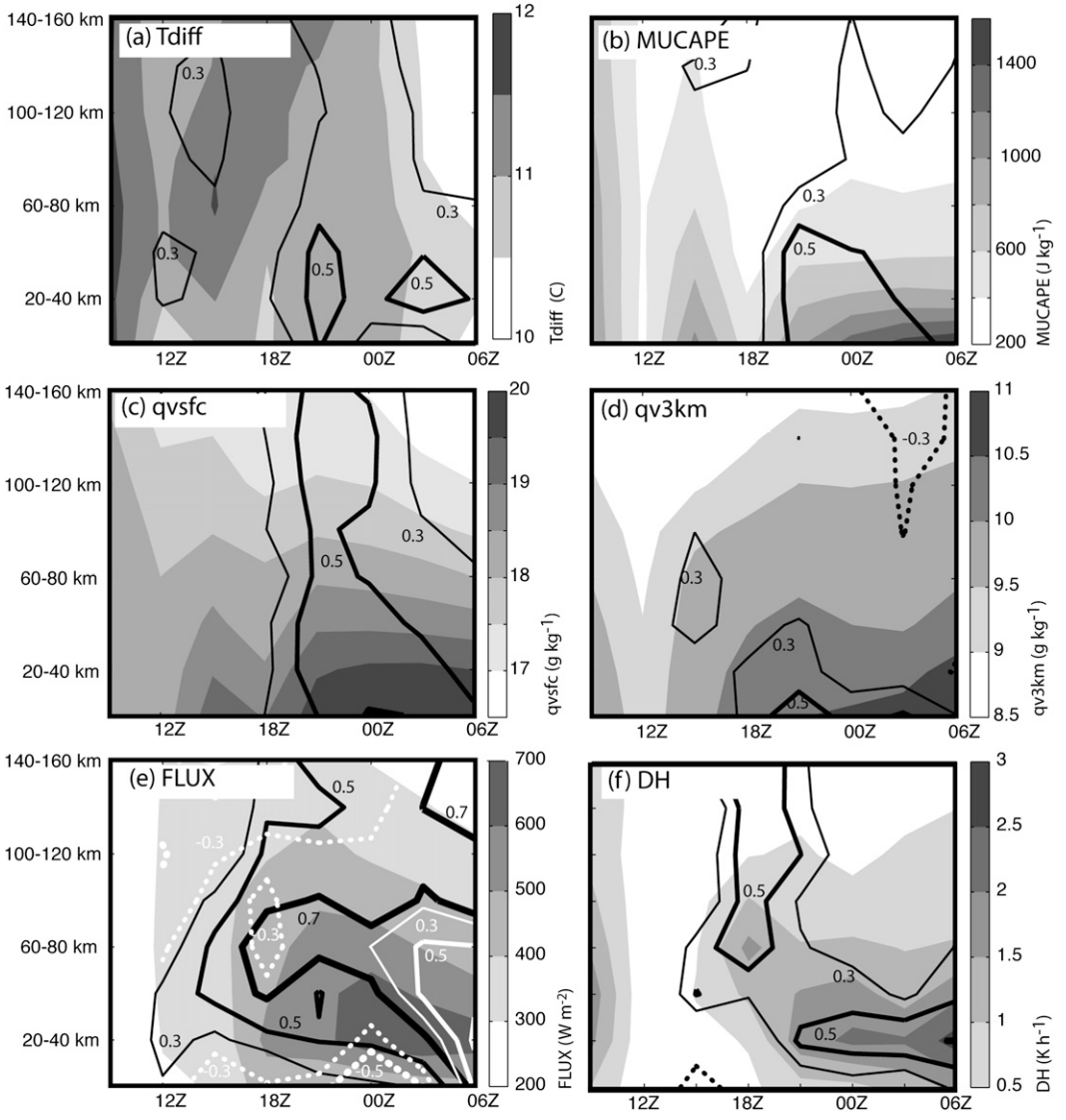

FIG. 10. The Lagrangian evolution of various ensemble-mean thermodynamic variables and their relationship with storm intensity: (a) T_{diff} (shaded every 0.5°C), (b) MUCAPE (shaded every 200 J kg^{-1}), (c) $q_{v\text{sfc}}$ (shaded every 0.5 g kg^{-1}), (d) $q_{v3\text{km}}$ (shaded every 0.5 g kg^{-1}), (e) total (latent + sensible) oceanic heat fluxes (FLUX, shaded every 100 W m^{-2}), and (f) 1–9-km average diabatic heating (DH, shaded every 0.5 K h^{-1}). In (a)–(d), the respective second-order part correlation with SLP_f (controlling for PV_1 and PRCP3h within the 5-mm isopleth) is contoured in black; (e) and (f) show the direct correlation with SLP_f. In addition, the correlation between FLUX and surface temperature is overlain in white in (e). Positive (negative) correlation is contoured in solid (dashed) lines at 0.3, 0.5, and 0.7 (−0.3, −0.5, −0.7) with increasing magnitude of correlation indicated by increasing line thickness. All variables are displayed as a function of radius and time from 0900 12 Sep to 0600 UTC 13 Sep and averaged in 20-km annuli before the correlation is computed.

gradients in moisture and temperature. Thus, for a storm with given latent heating and intensity, when surface temperature and low-level moisture are higher in this region, the strength of the cyclone is greater at 0600 UTC 13 September. Since the southern extent of the gradients marks the ensemble-mean leading edge of the slightly cooler and drier continental air, the correlation pattern implies that either a weaker front or greater distance between the cyclone and the continental air mass will result in a stronger cyclone. This suggests that the cyclones in some members ingest postfrontal air prior to 1800 UTC, which could hinder latent heating and the rate of genesis.

Aside from precipitation, another source of increasing PV is likely the data assimilation process. For example,

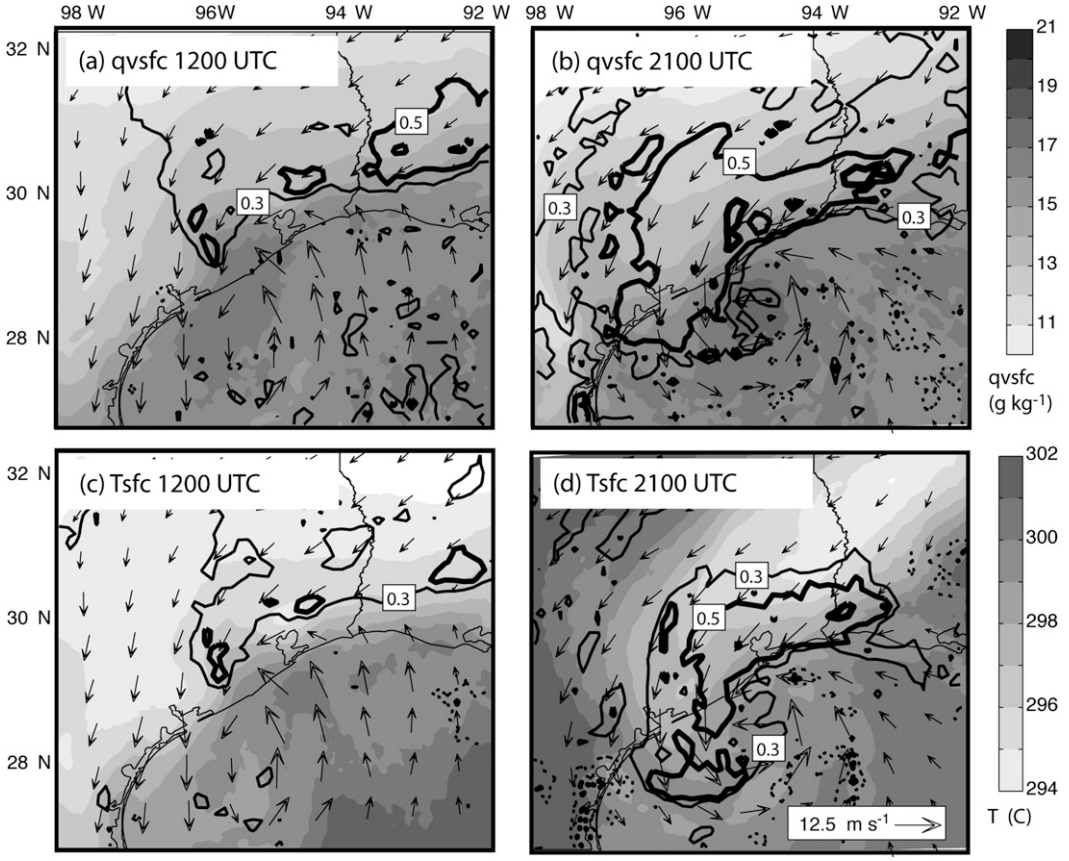

FIG. 11. Ensemble-mean Lagrangian (a),(b) q_{vsfc} (shaded every 1 g kg^{-1}), and (c),(d) T_{sfc} (shaded every 1°C) and their second-order part correlation with SLP_f at 1200 and 2100 UTC 12 Sep. Correlation is calculated controlling for PV_1 and PRCP3h within the 5-mm isopleth and contoured as in Fig. 10. Surface wind vectors are also shown. For spatial reference, the map background is plotted so that the circulation center is located at the ensemble-mean position of the cyclone.

data assimilation apparently increases low-level PV in the absence of convection between 1200 and 1500 UTC (Figs. 9b,c) and it likely continues to do so as convection intensifies after 1500 UTC. The extent to which data assimilation acts independent of ensemble dynamics to build the vortex is beyond the scope of this study.

b. Post–1800 UTC evolution

The previous subsection showed that spread in storm intensity is likely a result of differences in precipitation during the data assimilation period. Thus, any factors that influence precipitation in the storm genesis region, including low- to midlevel thermodynamics and the strength and position of the front to the north of the storm, also apparently affect intensity spread. Since precipitation variance after 1800 UTC continues to be a significant contributor to SLP_f spread (Fig. 8), we proceed by examining what factors act after 1800 UTC to affect precipitation and increase intensity spread even further.

1) FRONT–CYCLONE INTERACTION

The aforementioned uncertainty in the interaction between the cyclone and continental air more strongly affects ensemble spread between 1800 UTC 12 September and 0600 UTC 13 September. For example, between 1200 and 2100 UTC 12 September, in Fig. 11, the signal of negative correlation to front strength intensifies considerably and wraps around the north and west sides of the ensemble-mean cyclone. The signal reaches its peak strength at 2100 UTC, which is also when part correlation between PRCP3h and SLP_f is strongest (Fig. 8b). A similar pattern is also seen in Figs. 12a,b, which shows similar data to that of Fig. 11 for the MUCAPE and T_{diff} stability parameters. This implies that ingestion of cooler, drier, and more stable air hinders strengthening in some members and that less cyclone–front interaction is preferable for intensification.

Differences in storm track become increasingly relevant in determining the extent of cyclone–front interaction

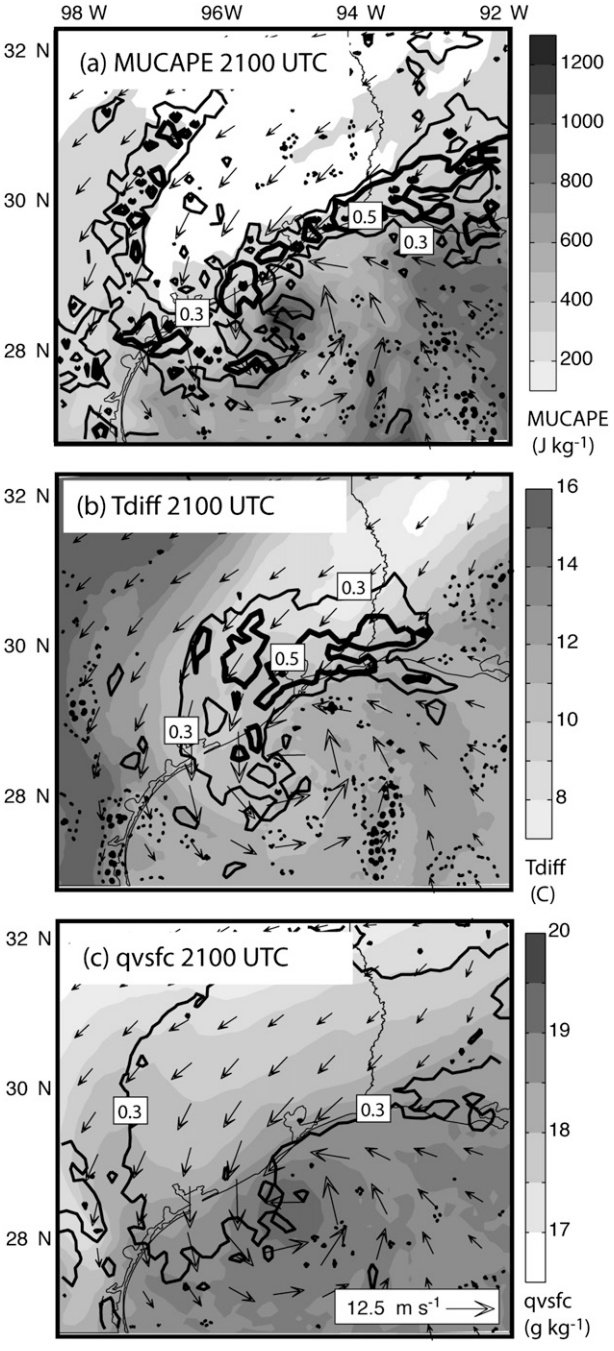

FIG. 12. As in Fig. 11 but for (a) MUCAPE (shaded every 100 J kg^{-1}) and (b) T_{diff} (shaded every 1°C) at 2100 UTC 12 Sep and (c) $q_{v\text{sfc}}$ (shaded every 0.5 g kg^{-1}) with correlation controlling for position as well as PV_1 and PRCP3h at 2100 UTC 12 Sep.

during the free forecast period. At and before 1800 UTC, track spread is fairly low because EnKF analyses adjust the cyclone position in all members toward the observed track. However, position spread increases substantially after 1800 UTC when the background wind is free to advect cyclones without track adjustment by the filter. In the present case, storm latitude varies much less than storm longitude, and longitude is best correlated with zonal mean wind only in the lowest kilometer (the magnitude of this correlation decreases quickly for mean wind over greater depths). In effect, storms surrounded by stronger 0–1-km westerly winds take a more easterly course parallel to the frontal boundary (e.g., member 8 in Fig. 1c), while those encompassed in stronger easterly flow move northwest toward the boundary (e.g., member 19 in Fig. 1c). The 2100 UTC result of larger track spread is a much stronger track-dependent difference in interaction between the cyclone and continental air. This is demonstrated in Fig. 13, where member 19 (Fig. 13b) has a cyclone that is visibly farther west and closer to the moisture gradient than that in member 8 (Fig. 13a). Thus, much of the intensity forecast uncertainty herein can be ascribed to differences in storm track near the decaying frontal boundary.

Differences in front strength also have some impact on cyclone intensity spread. To demonstrate this, Fig. 12c shows the part correlation between 2100 UTC $q_{v\text{sfc}}$ and SLP_f, controlling for position as well as PV_1 and PRCP3h. While adding the additional control for position reduces both the magnitude and areal extent of significant correlation (cf. Figs. 11b and 12c), there is still a fairly large region of weak correlation wrapping around the cyclone and inland over southeast Texas and Louisiana. This shows that, regardless of where a storm is or how strong it is, when the air over a large region near the storm is more moist, SLP_f is lower.

Figure 10 shows more clearly how frontal interaction relates to intensity in a mean sense. For example, from the 1800 UTC analysis through 0600 UTC, average $q_{v\text{sfc}}$ is moderately to strongly related to SLP_f (Fig. 10c). The relatively weaker and noisier signals for MUCAPE and T_{diff} in Fig. 12 are also reflected in their lower correlation in Figs. 10a,b. Meanwhile, except for within 20 km of the center, Fig. 10d shows that SLP_f seems to be less sensitive to 3-km moisture than to the other thermodynamic variables analyzed. As before, there is no consistent positive correlation between relative humidity and SLP_f (not shown).

Comparison of Fig. 14 with Figs. 1 and 13 illustrates how the aforementioned mechanisms apparently lead to an increasingly large difference between the cyclones in member 8 (Figs. 14a–c) and member 19 (Figs. 14d–f) from 2100 UTC 12 September to 0300 UTC 13 September. Member 8, which is much farther from the moisture gradient in Fig. 13, continues to have strong convection near the cyclone center. Meanwhile, most of the convection in member 19 is weaker and in a southwest–northeast oriented band well removed from the center. Thus, not

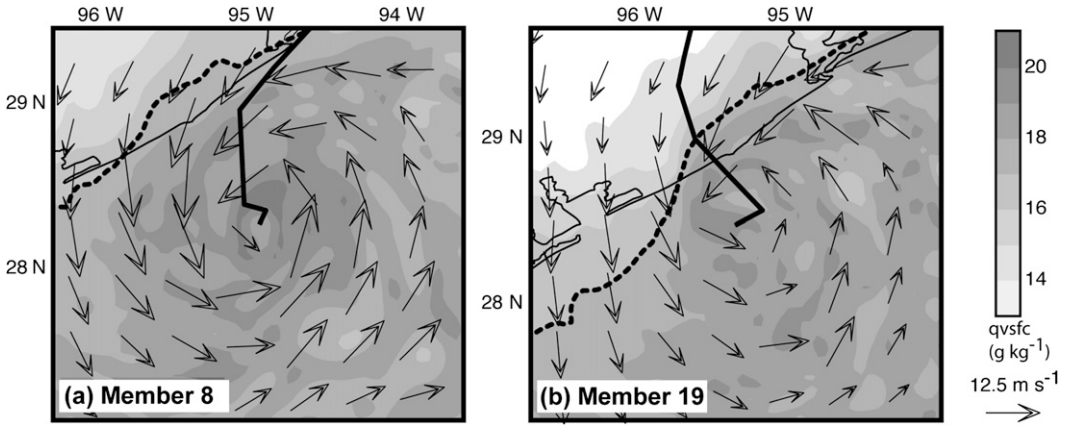

FIG. 13. Surface mixing ratio (shaded every 1 g kg^{-1}) and wind vectors are shown for members (a) 8 and (b) 19 at 2100 UTC 12 Sep. The approximate leading edge of dry, continental air is marked with a bold dashed line at the 17-g kg^{-1} isodrosotherm, and the track of the member in each panel is shown with a thick black line.

only is the member-8 cyclone stronger at 2100 UTC, but it strengthens more quickly between 2100 and 0300 UTC. This difference is similar to those between other ensemble members and continues in the ensemble beyond 0600 UTC 13 September. The result in terms of minimum SLP spread (i.e., standard deviation) is an increase from 1.6 to 3.3 hPa from 1800 UTC 12 September to 0600 UTC 13 September. Thus, uncertainty in the cyclone strength forecast more than doubles in this time period.

2) SURFACE MOISTURE VERSUS ATMOSPHERIC STABILITY

A serious question related to Figs. 10–12 is whether the measures of convective instability and surface moisture relate independently to intensification. All are moderately strong predictors of SLP_f but they are also strongly correlated to one another (not shown), and it is possible for the correlation between intensity and any of these variables to be a result of correlation between intensity

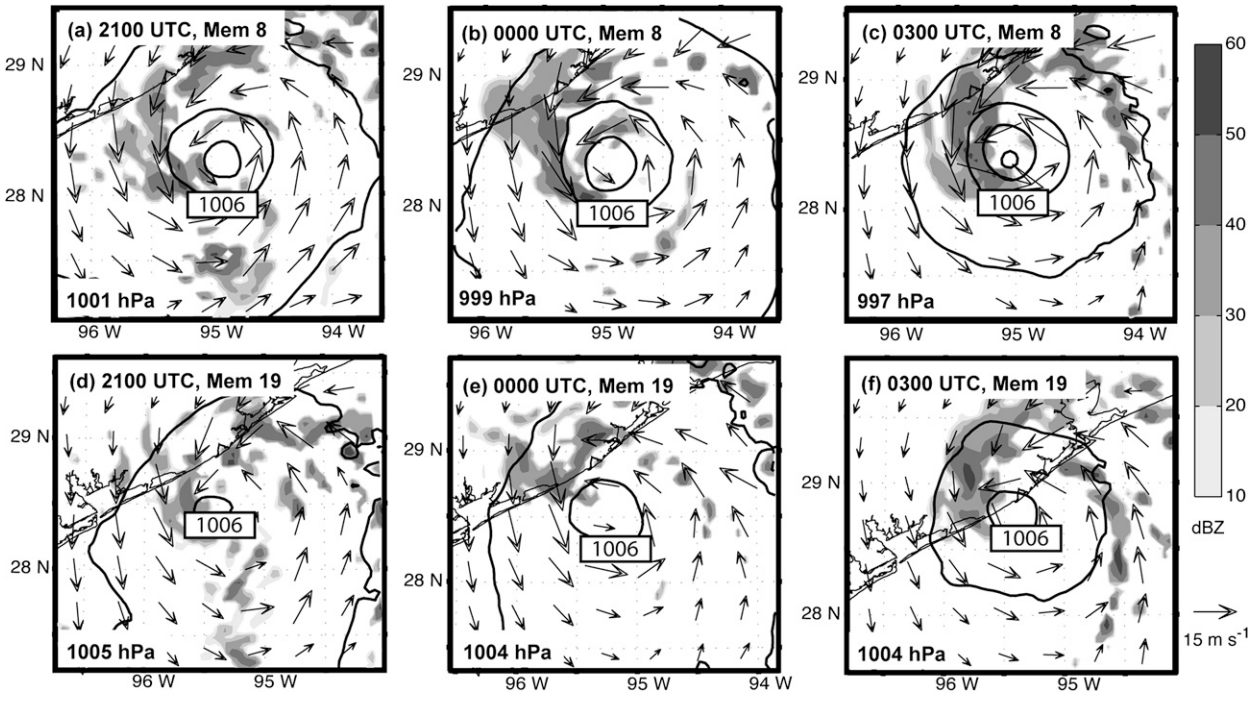

FIG. 14. The evolution of SLP (contoured at every 4 hPa), surface winds, and simulated radar reflectivity (shaded every 10 dBZ) for members (a)–(c) 8 and (d)–(f) 19. The minimum central pressure is indicated in the lower left corner of each panel.

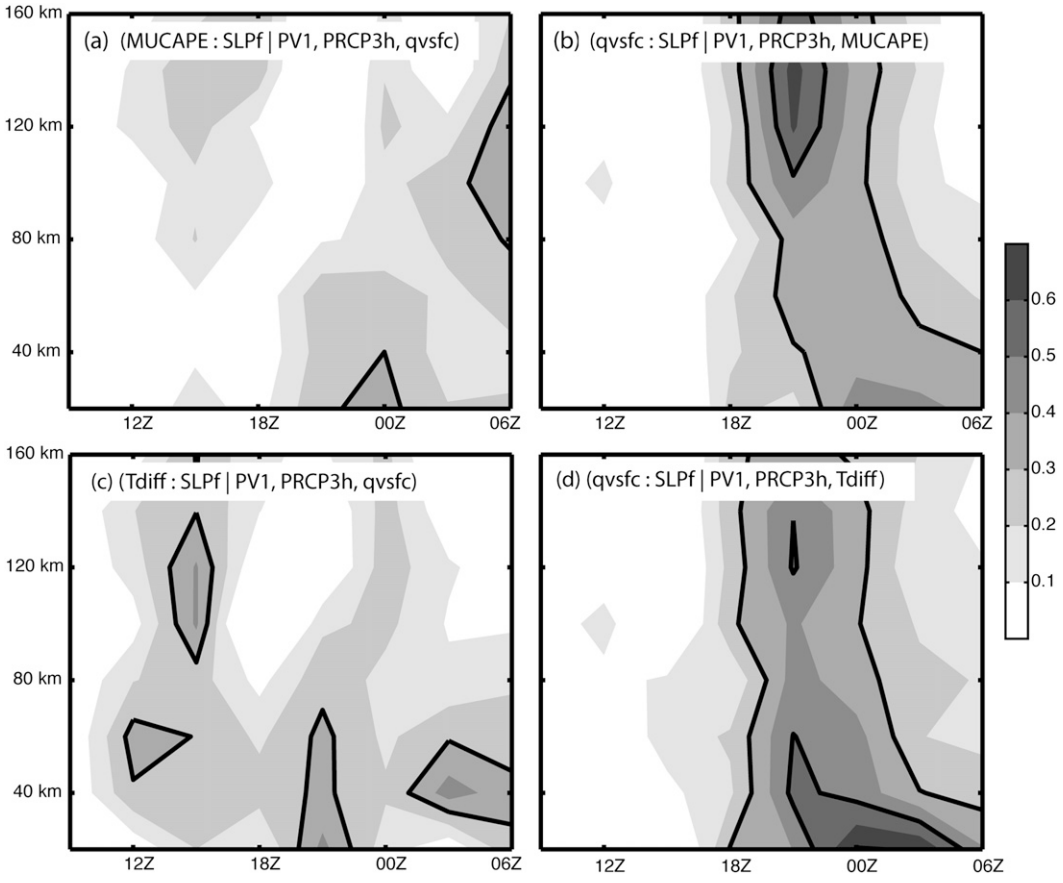

FIG. 15. The relationship between MUCAPE, T_{diff}, $q_{v\text{sfc}}$, and intensity. (a) Third-order part correlation between MUCAPE and SLP_f, controlling for $q_{v\text{sfc}}$, PRCP3h within the 5-mm isopleth and PV_1. (b) Part correlation between $q_{v\text{sfc}}$ and SLP_f controlling for MUCAPE, PRCP3h, and PV_1. (c) Part correlation between T_{diff} and SLP_f controlling for $q_{v\text{sfc}}$, PRCP3h, and PV_1. (d) Part correlation between $q_{v\text{sfc}}$ and SLP_f controlling for T_{diff} PRCP3h, and PV_1. Correlation is filled every 0.1 above 0.1, and thresholds of 0.3, 0.5, and 0.7 are indicated with bold lines.

and another one of these variables. Thus, statistical control is used in Fig. 15 to investigate how $q_{v\text{sfc}}$ and both MUCAPE and T_{diff} are independently correlated to SLP_f. All panels in Fig. 15 show considerable reduction in correlation compared to Figs. 10a–c, though this is expected since less variance remains after controlling for a variable [i.e., z_1 in Eq. (1)], that is highly correlated with the independent variable being tested [i.e., x in Eq. (1)]. Yet the relative magnitudes of part correlation in Fig. 15 are consistent with those in Fig. 10 and suggest that $q_{v\text{sfc}}$ is a more important contributor to intensification than either MUCAPE or T_{diff}. However, the remaining weak correlation in Figs. 15a,c implies that atmospheric stability is a secondary intensification factor. This result is generally similar to the finding in SZ08 that a deep layer of moist air is the most important contributor to genesis, and MUCAPE contributes to a lesser degree. Nevertheless, fully investigating the independent roles of moisture and atmospheric stability requires idealized experiments in which they are independently changed, which is beyond the scope of this study.

3) MATURE TROPICAL CYCLONE STAGE

Mature tropical cyclone dynamics appears to become active late on 12 September. One indication of the onset of such dynamics is the cessation of negative correlation between precipitation and surface temperature, which likely indicates diminishment of cold convective downdrafts (Rotunno and Emanuel 1987; Emanuel 1989) that are prevalent throughout much of 12 September. For example, in Fig. 16a surface temperatures downstream of the boxed area are weakly to moderately anticorrelated to mean precipitation within the boxed region. However, after about 2100 UTC anticorrelation between precipitation and downstream T_{sfc} ceases to be statistically significant (Fig. 16b), which reflects a similar trend seen also in an area-average sense (not shown). This change occurs absent significant correlation between low- to midlevel

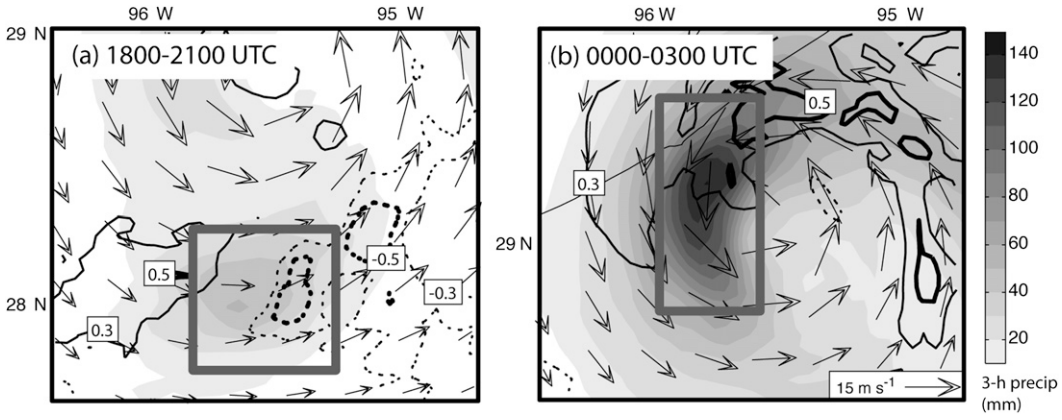

FIG. 16. Ensemble-mean precipitation (shaded every 10 mm) from (a) 1800 to 2100 UTC and (b) 0000 to 0300 UTC and correlation between surface temperature and area-average precipitation within the gray box. Correlation is contoured as in Fig. 10, and surface wind vectors are also shown. For spatial reference, the map background is plotted so that the circulation center is located at the ensemble-mean position of the cyclone.

relative humidity and SLP_f, which again suggests that variability in the humidity field does not influence downdraft intensity and drive spread in the ensemble. Instead, it seems more likely that downdrafts in all ensemble members weaken as mean relative humidity increases.

Other changes also signify a more mature mean cyclone by early 13 September. For example, oceanic heat fluxes and their correlation with SLP_f increase steadily through 12 September (Fig. 10e). Furthermore, at and before 0000 UTC 13 September the negative correlation between fluxes and T_{sfc} likely indicates that fluxes respond to cool downdrafts (Fig. 10e), which were shown to diminish after 0000 UTC. This is similar to the recovery period, observed in SZ08 and ZS09, in which surface heat fluxes helped the boundary layer to recover before the onset of more rapid intensification. Indeed, this correlation and the similar correlation between fluxes and q_{vsfc} (not shown) rapidly increase between 0000 and 0600 UTC (Fig. 10e), which shows that storms with stronger oceanic heat fluxes begin to have warm, moist surface air over a large area surrounding their centers. Storm organization also changes, and ensemble-mean latent heating and its correlation with SLP_f migrate radially inward and increase dramatically at a radius of 20–40 km between 1800 and 0000 UTC (Fig. 10f). This likely indicates an increase in organization of the core of the stronger storms in particular and possible formation of a partial eyewall and/or a strong primary rainband. Such formation is evident in member 8 by 0300 UTC (Fig. 14c).

The evolution to a mature tropical cyclone in many members increases existing spread. With the apparent weakening of downdrafts and enhanced fluxes in the strongest members easily modifying cooler surface air, convective instability near the center increases and provides a more favorable environment for heavy precipitation (Fig. 10b). The result that a storm can strengthen more quickly, as the deleterious effects of downdrafts decrease and fluxes increase, is an essential characteristic of mature tropical cyclone dynamics according to Rotunno and Emanuel (1987) and Emanuel (1989). Thus, mature storms in the ensemble strengthen more quickly than weaker storms, commencing mature tropical cyclone dynamics and marking a period of increasingly rapid intensification.

4) ENSEMBLE EVOLUTION AFTER 0600 UTC

Diversity in track continues increasing in importance after 0600 UTC as differing landfall times work with the previously described mechanisms to drive spread even higher. Because the airmass boundary lies parallel to the coast, varying landfall times act to increase existing differences in strength in the same sense as cyclone–front interaction. Strength spread due to landfall should obviously overwhelm the signal of the cyclone–front interaction as a substantial part of the ensemble begins to make landfall, but recall that all previous correlation analysis is constructed in a way that minimizes this by defining SLP_f at 0600 UTC 13 September. An example of the increased differences after 0600 UTC comes from comparing Figs. 1, 6, and 14. The cyclone in member 19 makes landfall between 0300 and 0600 UTC and weakens thereafter. Meanwhile, the storm in member 8 strengthens to a 34 m s^{-1} hurricane before making landfall between 1500 and 1800 UTC 13 September. In terms of the entire ensemble, minimum SLP spread approximately doubles again from 3.3 to 6 hPa between 0600 and 1200 UTC 13 September and continues to rapidly increase until storms in most members make landfall.

The obvious sensitivity of cyclone intensification in the ensemble to the track (because of both differing interaction with continental air and landfall times) is important for understanding predictability. As previously mentioned, the longitude of the cyclone is best related to the mean zonal wind in the lowest 1 km. In fact, the 200-km track envelope at 1200 UTC 13 September can largely be explained by the maximum difference among ensemble members in mean 1-km zonal winds surrounding the cyclone, which averages around 2.5–3.0 m s^{-1} during the free forecast. What makes this so interesting is that the approximately 0.75 m s^{-1} spread in the 1-km zonal wind component near the cyclone is about half of NCEP-assumed rawinsonde observation error at the same level (1.5 m s^{-1}). SZ08 and ZS09 showed that analysis error in marine environments can rival or exceed rawinsonde error, so differences in wind less than typical observation or analysis error can result in track differences that control whether or not a hurricane forms in as little as 18 h. This is reminiscent of the results of ZS09, which also found that very small differences in initial conditions can determine whether or not a tropical cyclone develops.

5) VERTICAL WIND SHEAR

Vertical wind shear is also known to inhibit genesis, so its relation to intensification in the ensembles is also briefly mentioned here. Mean shear within 300 km of the center (measured through multiple levels, not shown) is fairly weak during the entire period, and there is no consistent signal of significant part correlation between shear and SLP_f. Thus, it does not appear that shear has an impact on ensemble spread here.

6. Summary and discussion

Using a WRF-EnKF analysis system and an ensemble forecast initialized with EnKF perturbations from Zhang et al. (2009), this study has investigated mechanisms leading to the extreme forecast uncertainty associated with Hurricane Humberto (2007). Humberto rapidly formed off the upper Texas coast and posed significant intensity forecast problems before its landfall less than a day later. In this study, similar methodology to that of SZ08 is used to investigate why storms in some ensemble members rapidly form a hurricane and others do not. This research presents a considerable improvement upon SZ08 owing to use of the hot-start EnKF analysis technique and because the storm in the present study develops, whereas SZ08 is a null case without observed development.

Strength differences during the analysis period, before 1800 UTC 12 September, are related to differences in precipitation, which themselves appear to originate due to differences in low-level convective instability, midlevel moisture, and a weak surface front to the north of the developing cyclone. Variance in precipitation begins to influence strength spread as early as 1100 UTC and continues to do so through the morning. In the presence of heavy precipitation, ensemble-mean PV increases, as does the correlation between PV and later storm intensity. Meanwhile, ensemble members with greater low-level convective instability, midlevel moisture, and a weaker front during these same periods have cyclones that strengthen more quickly. Although the relationship between midlevel moisture and cyclone intensification is consistent with the long-held belief that ample moisture through a deep layer is necessary for tropical cyclone development, more caution must be taken in interpreting the sensitivity to stability, particularly early in the analysis period. It is possible, especially early during the assimilation period, that adjustments associated with the data assimilation cycles result in artificial sensitivity to atmospheric stability. However, such adjustments tend to decrease when cycling is used to produce analyses (e.g., Snyder and Zhang 2003; Zhang et al. 2004), and the dynamics inferred nearer 1800 UTC are less likely to be unreliable. Finally, the negative relationship between cyclone intensity and the strength of the front implies that some ensemble members ingest cooler, drier continental air before 1800 UTC, which hinders intensification.

Increasing spread early in the free forecast period is strongly related to differences in the interaction between cyclones and the continental air to the north. Varying surface moisture and convective instability near the cyclone, related to both the strength of the front and proximity of the cyclone to the remnant front, appear to result in different cyclone intensification rates and a doubling of minimum SLP spread between 1800 UTC 12 September and 0600 UTC 13 September. owing to a strong relationship between convective instability and surface moisture, it is difficult to precisely determine the extent to which they act independently to promote intensification. However, the results here suggest that low-level moisture is the primary intensification mechanism and that atmospheric stability augments changes in strength.

Ensemble statistics also suggest that several other factors act in concert with front–cyclone interaction to drive spread even higher on 13 September. First, the increase in oceanic heat fluxes and diminishment of cold downdrafts are among a number of statistical and mean changes that imply the commencement of mature tropical cyclone dynamics in many ensemble members around 0000 UTC. With such dynamics in place, stronger cyclones intensify more rapidly than weaker cyclones, thus increasing spread. Second, storms in many ensemble members begin to make landfall after 0600 UTC. Since the coastline also marks the boundary of continental air, varying landfall

time increases spread in the same sense of differing interaction between the cyclone and continental air. Of course, the impact of landfall is much more severe and likely becomes the dominant mechanism for increasing spread after 0600 UTC. With multiple mechanisms acting to increase spread during this later period, its rate of increase becomes considerably faster than on 12 September.

These results are important because they generally confirm the main findings of SZ08. Although the ensemble initialization method, the genesis environment, and the storm itself are very different here than in SZ08, ensemble statistics again suggest that moisture and convective instability modulate the rate of intensification. Curiously, in both studies variability in moisture seems to be most important for its direct impact upon latent heating and not because of any variance in cold downdraft mitigation. The increase in spread due to the commencement of mature tropical cyclone dynamics is also similar to the findings of SZ08. As in SZ08, these results justify the inclusion of a convective instability metric as a secondary parameter that can modulate the rate of intensification, such as in the SHIPS model (e.g., DeMaria et al.2005). Results here might also support the idea of Montgomery et al. (2006) that CAPE enhances genesis by feeding vortical hot towers, though the relationship between VHTs and net latent heating is not clear at this point.

One of the most intriguing results of this study is the extreme sensitivity to very small changes in initial conditions. This is best demonstrated by the sensitivity to cyclone track, which controls much of the sensitivity to front–cyclone interaction and all of the sensitivity to landfall time. In particular, storm longitude seems to be more relevant than latitude because it shows considerably more variance among ensemble members. Storm longitude is well correlated with the mean low-level zonal wind surrounding the cyclone, and differences in mean wind seem to explain the observed track envelope quite well. What is so alarming is that spread in zonal wind surrounding the cyclone is only 0.5–0.75 m s^{-1}, which is considerably less than NCEP-assumed rawinsonde error and potentially less than analysis error in a marine environment. Thus, in certain circumstances, differences in initial conditions smaller than observational or analysis uncertainty can strongly modulate the extent to which a tropical cyclone develops. This result is very similar to that of ZS09, which found that error far smaller than can be detected by any analysis or observation system can determine whether or not a tropical cyclone will form. The very large spread in this case further demonstrates the limit of practical predictability of hurricane intensity, discussed in ZS09, and illustrates the need for developing advanced ensemble prediction systems to provide event-dependent probabilistic forecasts and risk assessment.

Acknowledgments. This research started as part of the first author's doctoral dissertation at Texas A&M University and continued during the author's tenure at NASA's Goddard Space Flight Center under the NASA Postdoctoral Program. The authors have benefited from discussions with John Nielsen-Gammon, Scott Braun, and Larry Carey. Thanks are also due to Yonghui Weng for help on the ensemble simulation. Finally, the authors appreciate comments that significantly improved this study from *Journal of the Atmospheric Sciences* editor Shigeo Yoden, reviewer Ron McTaggart-Cowan, and two anonymous reviewers. Research completed at Texas A&M University was sponsored in by the U.S. Office of Naval Research under Grants N000140410471 and N000140910526 and by NSF Grant ATM-084065. The remaining work, completed under the NASA Postdoctoral Program, was sponsored by Oak Ridge Associated Universities through a contract with NASA.

REFERENCES

Bei, N., and F. Zhang, 2007: Impacts of initial condition errors on mesoscale predictability of heavy precipitation along the mei-yu front in China. *Quart. J. Roy. Meteor. Soc.,* **133,** 83–99.

Bender, M. A., I. Ginis, and Y. Kurihara, 1993: Numerical simulations of tropical cylone–ocean interaction with a high-resolution coupled model. *J. Geophys. Res.,* **98,** 23 245–23 263.

Black, P. G., 1983: Ocean temperature changes induced by tropical cyclones. Ph.D. dissertation, The Pennsylvania State University, 278 pp.

Cecil, D. J., and E. J. Zipser, 1999: Relationships between tropical cyclone intensity and satellite-based indicators of inner core convection: 85-GHz ice-scattering signature and lightning. *Mon. Wea. Rev.,* **127,** 103–123.

DeMaria, M., J. A. Knaff, and B. H. Connell, 2001: A tropical cyclone genesis parameter for the tropical Atlantic. *Wea. Forecasting,* **16,** 219–233.

——, M. Mainelli, L. K. Shay, J. A. Knaff, and J. Kaplan, 2005: Further improvements to the Statistical Hurricane Intensity Prediction System (SHIPS). *Wea. Forecasting,* **20,** 531–543.

Doswell, C. A., III, and E. N. Rasmussen, 1994: The effect of neglecting the virtual temperature correction on CAPE calculations. *Wea. Forecasting,* **9,** 625–629.

Elsberry, R. L., T. D. B. Lambert, and M. A. Boothe, 2007: Accuracy of Atlantic and eastern North Pacific tropical cyclone intensity forecast guidance. *Wea. Forecasting,* **22,** 747–762.

Emanuel, K. A., 1986: An air–sea interaction theory for tropical cyclones. Part I: Steady-state maintenance. *J. Atmos. Sci.,* **43,** 585–605.

——, 1989: The finite-amplitude nature of tropical cyclogenesis. *J. Atmos. Sci.,* **46,** 3431–3456.

Franklin, J. L., 2005: 2004 National Hurricane Center forecast verification report. NHC, 46 pp. [Available online at http://www.nhc.boulder.noaa.gov/verification/pdfs/Verification_2004.pdf.]

Hakim, G. J., and R. D. Torn, 2008: Ensemble synoptic analysis. *Synoptic–Dynamic Meteorology and Weather Analysis and Forecasting: A Tribute to Fred Sanders, Meteor. Monogr.,* No. 55, Amer. Meteor. Soc., 147–162.

Hawblitzel, D. P., F. Zhang, Z. Meng, and C. A. Davis, 2007: Probabilistic evaluation of the dynamics and predictability of the mesoscale convective vortex of 10–13 June 2003. *Mon. Wea. Rev.,* **135,** 1544–1563.

Haynes, P. H., and M. E. McIntyre, 1987: On the evolution of vorticity and potential vorticity in the presence of diabatic heating and frictional or other forces. *J. Atmos. Sci.,* **44,** 828–841.

Hendricks, E. A., M. T. Montgomery, and C. A. Davis, 2004: The role of ''vortical'' hot towers in the formation of Tropical Cyclone Diana (1984). *J. Atmos. Sci.,* **61,** 1209–1232.

Houze, R. A., S. S. Chen, B. F. Smull, W. C. Lee, and M. M. Bell, 2007: Hurricane intensity and eyewall replacement. *Science,* **315,** 1235–1238.

Islam, S., R. L. Bras, and K. A. Emanuel, 1993: Predictability of mesoscale rainfalls in the tropics. *J. Appl. Meteor.,* **32,** 297–310.

Kerns, B., and E. Zipser, 2009: Four years of tropical ERA-40 vorticity maxima tracks. Part II: Differences between developing and nondeveloping disturbances. *Mon. Wea. Rev.,* **137,** 2576–2591.

Montgomery, M. T., M. E. Nichols, T. A. Cram, and A. Saunders, 2006: A vortical hot tower route to tropical cyclogenesis. *J. Atmos. Sci.,* **63,** 355–386.

Nolan, D., E. D. Rappin, and K. A. Emanuel, 2007: Tropical cyclogenesis sensitivity to environmental parameters in radiative–convective equilibrium. *Quart. J. Roy. Meteor. Soc.,* **133,** 2085–2107.

Olson, D. A., N. W. Junker, and B. Korty, 1995: Evaluation of 33 years of quantitative precipitation forecasting at the NMC. *Wea. Forecasting,* **10,** 498–511.

Rotunno, R., and K. A. Emanuel, 1987: An air–sea interaction theory for tropical cyclones. Part II: Evolutionary study using a nonhydrostatic axisymmetric numerical model. *J. Atmos. Sci.,* **44,** 542–561.

Sippel, J. A., and F. Zhang, 2008: A probabilistic analysis of the dynamics and predictability of tropical cyclogenesis. *J. Atmos. Sci.,* **65,** 3440–3459.

Snyder, C., and F. Zhang, 2003: Assimilation of simulated Doppler radar observations with an ensemble Kalman filter. *Mon. Wea. Rev.,* **131,** 1663–1677.

Torn, R. D., 2010: Ensemble-based sensitivity analysis applied to African easterly waves. *Wea. Forecasting,* **25,** 61–78.

Van Sang, N., R. K. Smith, and M. T. Montgomery, 2008: Tropical-cyclone intensification and predictability in three dimensions. *Quart. J. Roy. Meteor. Soc.,* **134,** 563–582.

Zhang, F., 2005: Dynamics and structure of mesoscale error covariance of a winter cyclone estimated through short-range ensemble forecasts. *Mon. Wea. Rev.,* **133,** 2876–2893.

——, and J. A. Sippel, 2009: Effects of moist convection on hurricane predictability. *J. Atmos. Sci.,* **66,** 1944–1961.

——, C. Snyder, and R. Rotunno, 2002: Mesoscale predictability of the ''surprise'' snowstorm of 24–25 January 2000 *Mon. Wea. Rev.,* **130,** 1617–1632.

——, ——, and ——, 2003: Effects of moist convection on mesoscale predictability. *J. Atmos. Sci.,* **60,** 1173–1185.

——, ——, and J. Sun, 2004: Impacts of initial estimate and observation availability on convective-scale data assimilation with an ensemble Kalman filter. *Mon. Wea. Rev.,* **132,** 1238–1253.

——, A. M. Odins, and J. W. Nielsen-Gammon, 2006: Mesoscale predictability of an extreme warm-season precipitation event. *Wea. Forecasting,* **21,** 149–166.

——, N. Bei, R. Rotunno, C. Snyder, and C. C. Epifanio, 2007: Mesoscale predictability of moist baroclinic waves: Convection-resolving experiments and multistage error growth dynamics. *J. Atmos. Sci.,* **64,** 3579–3594.

——, Y. Weng, J. A. Sippel, Z. Meng, and C. H. Bishop, 2009: Cloud-resolving hurricane initialization and prediction through assimilation of Doppler radar observations with an ensemble Kalman filter. *Mon. Wea. Rev.,* **137,** 2105–2125.